ChemComm

COMMUNICATION

View Article Online
View Journal | View Issue

Cite this: *Chem. Commun.*, 2017, 53, 1700

Received 28th September 2016,
Accepted 12th January 2017

DOI: 10.1039/c6cc07878h

www.rsc.org/chemcomm

Structure, transport and photoconductance of PbS quantum dot monolayers functionalized with a copper phthalocyanine derivative†

A. André,[a] C. Theurer,[a] J. Lauth,[b] S. Maiti,[c] M. Hodas,[c] M. Samadi Khoshkhoo,[a] S. Kinge,[d] A. J. Meixner,[ae] F. Schreiber,[ce] L. D. A. Siebbeles,[b] K. Braun[a] and M. Scheele*[ae]

We simultaneously surface-functionalize PbS nanocrystals with Cu 4,4′,4″,4‴-tetraaminophthalocyanine and assemble this hybrid material into macroscopic monolayers. Electron microscopy and X-ray scattering reveal a granular mesocrystalline structure with strong coherence between the atomic lattice and the superlattice of nanocrystals within each domain. Terahertz spectroscopy and field-effect transistor measurements indicate efficient coupling of holes throughout the hybrid thin film, in conjunction with a pronounced photoresponse. We demonstrate the potential of this material for optoelectronic applications by fabricating a light-effect transistor.

Combining semiconductor nanocrystals (NC) and organic semiconductor molecules into coupled organic–inorganic nanostructures (COIN) gives access to hybrid materials with entirely new properties.[1–5] To name only a few, some key questions in COIN materials involve the nature of the exciton (Frenkel or Wannier–Mott type), the speed of charge transfer across the organic/inorganic interface, the tunability of electronic coupling *via* the quantum size effect as well as the efficiency of singlet fission.[6–9] In particular, COINs based on PbS nanocrystals have demonstrated excellent potential for applications as photodetectors.[9–11] In the same context, the photoconductivity in metal phthalocyanines, its selective response to vapour and the application as molecular noses have been extensively studied.[12,13] Thus, we see great potential for a hybrid material comprising of well-dispersed PbS NCs and phthalocyanines with many frequent interfaces for optoelectronic applications. In addition, the energies of the first excited hole state in PbS NCs and the highest occupied molecular orbital in Pcs are rather similar which bears the prospect of resonant coupling for holes in this hybrid material.[14,15]

In this work, we develop a chemical procedure to fabricate ordered monolayers of PbS NCs surface-functionalized with Cu 4,4′,4″,4‴-tetraaminophthalocyanine (Cu-4APc). We monitor the ligand exchange at the NC surface, characterize the structure of the hybrid film, measure important electric transport parameters and assess the potential of this COIN for photodetection.

Thin films of oleic acid-capped PbS NCs are assembled at the liquid/air interface and simultaneously ligand-exchanged with Cu-4APc in a closed cell, using acetonitrile as the liquid substrate. (For details, the reader is referred to the ESI† unit.) The surface-functionalization with Cu-4APc is verified *via* X-ray photoemission spectroscopy (XPS) and vibrational spectroscopy (FT-IR) (see Fig. S1 in the ESI† unit).

The real-space structure of Cu-4APc functionalized PbS NC thin films is characterized by transmission and scanning electron microscopy (TEM and SEM) in Fig. 1. The fast Fourier transform (FFT) of a single superlattice domain (Fig. 1a and inset) indicates structural coherence between the (200) atomic lattice planes of the PbS NCs (3.4 nm^{-1} in reciprocal space). This is supported by the high-resolution TEM image in Fig. 1b bearing mainly the typical (200) lattice spacing of 3 Å. The low-magnification SE micrograph in Fig. 1c indicates that structural coherence is also preserved over length scales on the order of micrometers. In terms of the film morphology, the TE micrographs in Fig. 1a and b indicate a mostly mono-layered structure with average particle spacing of 1.3 nm to 1.5 nm, which matches the estimated length of a Cu-4APc molecule. Fig. 1d depicts a typical PbS-Cu4APc thin film with an area of approx. 100 μm^2, smooth surface and almost no voids.

For a macroscopically averaged characterization of the structural properties of Cu-4APc functionalized PbS NC thin

[a] *Institute of Physical and Theoretical Chemistry, University of Tübingen, Auf der Morgenstelle 18, 72076 Tübingen, Germany. E-mail: marcus.scheele@uni-tuebingen.de*
[b] *Chemical Engineering Department, Delft University of Technology, Van der Maasweg 9, 2619 HZ Delft, The Netherlands*
[c] *Institute of Applied Physics, University of Tübingen, Auf der Morgenstelle 10, 72076 Tübingen, Germany*
[d] *Toyota Motor Europe, Materials Research & Development, Hoge Wei 33, B-1930, Zaventem, Belgium*
[e] *Center for Light-Matter Interaction, Sensors & Analytics LISA+, University of Tübingen, Auf der Morgenstelle 15, 72076 Tübingen, Germany*

† Electronic supplementary information (ESI) available: Materials and methods. (S1) XPS and FT-IR characterization of ligand exchange. (S2) Size histogram of PbS nanocrystals. (S3) Description of the cell used for self-assembly. (S4) GISAXS Fit. (S5) XRR and density profile. (S6–S10) Description of the confocal microscopy set-up. See DOI: 10.1039/c6cc07878h

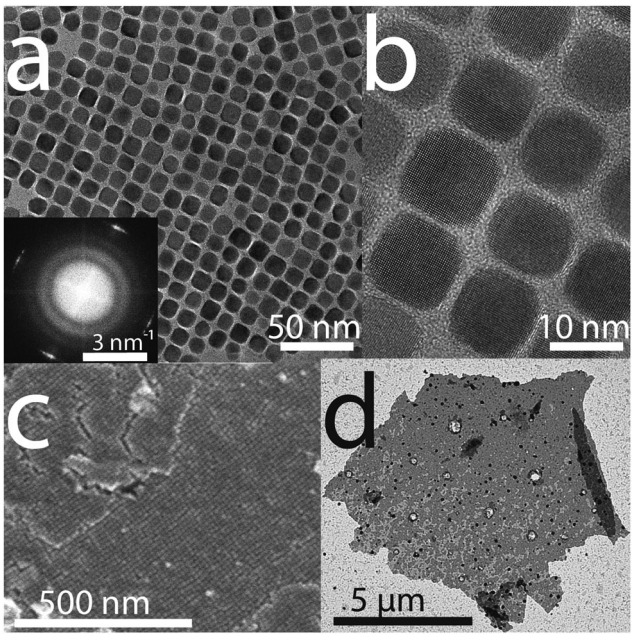

Fig. 1 (a) Transmission electron micrograph of a typical Cu-4APc functionalized PbS NC film. The inset represents the FFT of the same image; the four white spots at 3.4 nm^{-1} represent the 200 PbS lattice planes. (b) High-resolution TEM of the same NC film. (c) Scanning electron micrograph of a similar NC film showing long-range structural coherence. (d) Low-magnification micrograph of a thin film.

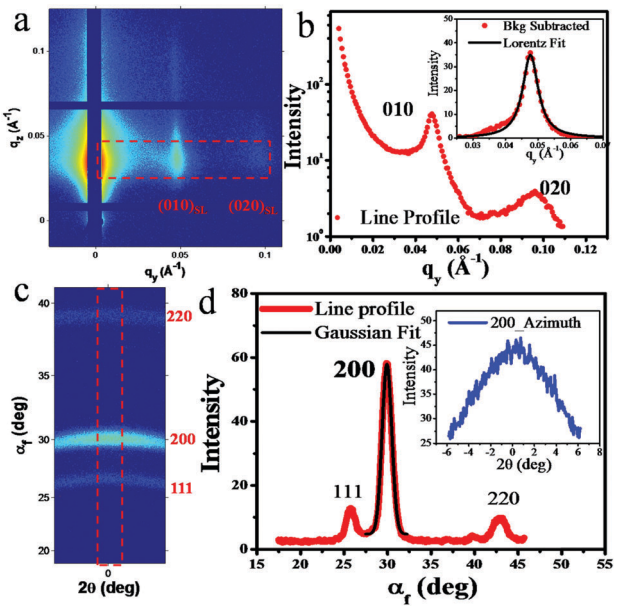

Fig. 2 (a) GISAXS of a typical Cu-4APc functionalized PbS NC film. The image is indexed on the assumption of a [001] zone axis. (b) The extracted line profiles from the GISAXS image as a function of in-plane wave vector q_y (red dotted box). Inset: Background subtracted 010 peak and its Lorentz fit. (c) GIWAXS image of the same film obtained by employing a 100 K Pilatus detector. The peaks are indexed according to the atomic lattice of rock salt PbS. (d) The extracted line profile of the GIWAXS image along the out-going angle α_f (red dotted box). Inset: Azimuthal profile of the 200 atomic lattice peak.

films, we perform simultaneous grazing incidence small-angle and wide-angle X-ray scattering (GISAXS and GIWAXS) as well as X-ray reflectivity (XRR) measurements. The GISAXS image (Fig. 2a) and its extracted line profile (Fig. 2b) as a function of the in-plane wave vector q_y show in-plane correlation peaks at q_y = 0.0475 Å^{-1}, and its higher order at q_y = 0.0953 Å^{-1}, indicating the formation of a highly ordered two-dimensional (2D) cubic superlattice. These values correspond to an average lattice spacing and domain size of approx. 13.2 nm ($\zeta = 2\pi/q_y$) and 110 nm, respectively. GIWAXS data (Fig. 2c) and its extracted line profile (Fig. 2d) shows the 111, 200 and 220 diffraction peaks of the PbS atomic lattice. The "arc" like 200 Bragg peak and its finite azimuthal angular distribution (inset of Fig. 2d) indicates significant angular correlation between the planes in the superlattice and the atomic lattice of PbS. This supports the real-space analysis in Fig. 1, but on a much larger scale (the typical footprint is on the order of 500 μm). In addition, XRR data on the same film (ESI† unit, Fig. S3) is in good agreement with a single layer of PbS-Cu4APc.

The electrical transport properties of Cu4APC functionalized PbS NC monolayers are assessed by AC and DC transport characterization, using transient terahertz (THz) spectroscopy and field-effect transistor (FET) measurements, respectively, in Fig. 3. The laser system used for THz conductivity measurements has been described earlier and data acquisition and evaluation is briefly discussed in the ESI† unit.[16–18] Fig. 3a shows time-resolved THz measurements of Cu-4APc functionalized PbS NC films. The plotted function $S(t) = \Phi_e(t)\mu_e + \Phi_h(t)\mu_h$ with the time t after photoexcitation at 800 nm includes the sum of the product

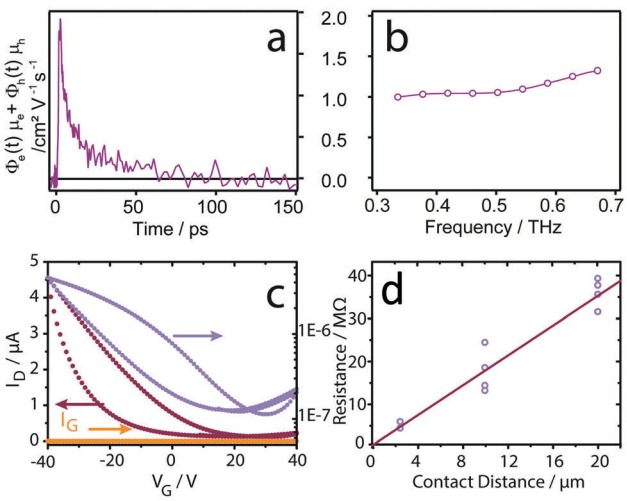

Fig. 3 (a) Sum of the product of the quantum yield Φ of electrons and holes in PbS NCs functionalized with Cu-4APc and the real part of the mobility, averaged over a frequency range of 0.3–0.7 THz at photoexcitation density of 3.3 × 10^{14} cm^{-2}. (b) Frequency dependence of the charge mobility in photoexcited PbS-Cu-4APc films. (c) Linear and semi-log presentation of the transconductance of a typical Cu-4APc functionalized PbS NC film at a constant drain voltage of +5 V. The negligible gate leakage is also displayed. (d) Plot of the total resistance *vs.* channel length in a typical FET. The contact resistance is extracted by a linear fit to this data as detailed in the text.

of the quantum yield of electrons, $\Phi_e(t)$ and holes, $\Phi_h(t)$, and the real mobility component of their mobility, (μ_e and μ_h), averaged over a frequency range of 0.3–0.7 THz. After peaking at early

times of the measurement during which hot charge carriers relax to the band edge ($\leq$4 ps), the THz conductivity yields $S(t)$ = 1 cm^2 V^{-1} s^{-1} (photoexcitation density N_a = 3.3 $\times$ 10^{14} photons per cm^2). The sum of the electron and hole mobility as a function of frequency (after relaxation of hot charges, time interval 8–12 ps) is additionally shown in Fig. 3b. The increase of the mobility with frequency is a typical sign for backscattering of mobile charges.

FET gate sweeps between −40 V to 40 V (Fig. 3c) reveal mostly unipolar hole conduction with threshold voltages of 10–20 V. Using the gradual channel approximation in the linear regime, we derive an FET hole mobility on the order of 10^{-3} cm^2 V^{-1} s^{-1}. The typical concentration of free holes is on the order of 10^{17} cm^{-3}.

Significantly higher mobilities probed by time-resolved THz spectroscopy can be explained by the short time- and length-scales over which the THz conductivity is determined ($\sim$1 ps, $<$5 nm).[19] In this respect, THz conductivity is not sensitive to charge carrier scattering over longer distances and represents the intrinsic upper limit for charge transport.[20] Possible reasons for carrier scattering under the conditions applied in FET measurements include contact resistance, defect/trap state-mediated scattering as well as scattering at grain boundaries. To verify whether contact resistance inhibits the FET performance, we apply the transmission line method (TLM) by measuring and linear fitting of the total resistance for varying contact distances. The y-axis intercept and slope in Fig. 3d yield the contact resistance and channel sheet resistance of the FET, respectively.[21] The extracted contact resistance is orders of magnitude lower than the active layer's sheet resistance, indicating that its effect on the device is negligible.

The large extinction coefficients of PbS NCs and Cu4APc lead to strong optical absorption through the visible regime (400–700 nm) with various resonances, which we seek to exploit for constructing a Light Effect Transistors (LET).[22] Such a device works similarly to an FET but instead of a gate voltage, light illumination is used to modulate the current flow.[23] Fig. 4 displays photocurrent measurements performed on PbS-Cu-4APc thin films with a stage-scanning confocal microscope equipped with a 633 nm laser (for more details see the ESI† unit).[24] The luminescence image (Fig. 4a) shows the two electrodes and the illuminated channel. On gold, the luminescence of the NC monolayer is quenched and the electrodes appear dark, while on glass a weak signal is detected. We assume that the very low quantum efficiency of the optically excited states on glass is due to efficient charge carrier separation inside the NC monolayer. This phenomenon is a promising property for the optical driven current flow. For each point in the optical image the current is measured as well, resulting in a current image (Fig. 4b). We find that the current undergoes strong modulation by illuminating the junction. To verify this, we measure charge carrier transport across the channel with different optical intensities (Fig. 4c) at a constant bias of 3 V. For each intensity, an image is taken and a line section at the same location is displayed. We also determine the dark current for the junction by blocking the laser. With the confocal microscope, only a small sample area (500 nm^2) is illuminated. Furthermore, the current is fluctuating along the junction, due to contact

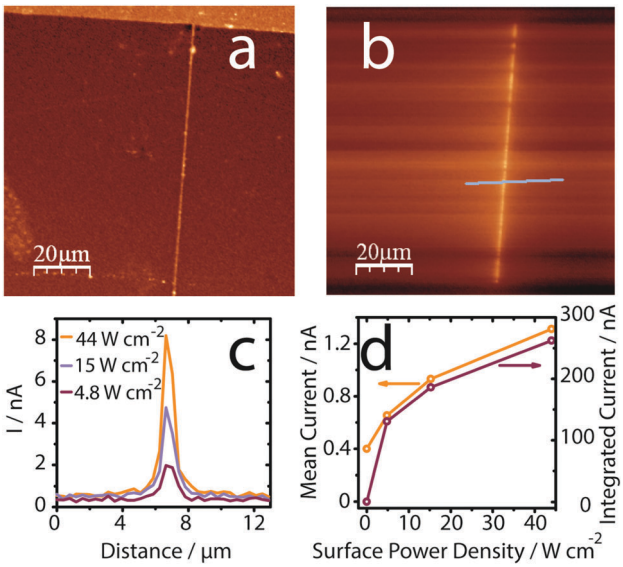

Fig. 4 Confocal photocurrent measurement on a Cu-4APc functionalized PbS NC film, deposited on gold electrodes with a separation of $\sim$250 nm. Simultaneously to the photoluminescence image (a) a current image is acquired (b). Both images clearly show the channel and an increased current flow when the trench is illuminated. (c) Plot of linecuts over the channel with different illumination intensities. (d) Averaged current over a single spot and integrated current flow over the whole junction.

discrepancies from the NC monolayer to the gold electrodes. Therefore, we calculate the averaged current and in addition the integrated current for the complete device (Fig. 4d). For the full device we obtain an I_{On}/I_{Off} ratio of $\leq$250.

Simultaneous self-assembly and ligand exchange of NCs at the liquid–air interface is a powerful means to obtain macroscopic monolayers with pronounced long-range order of NCs. On a shorter range (approx. 110 nm on average), strong iso-orientation of the atomic lattices of individual NCs with the superlattice of NCs is achieved such that these films can be described as granular mesocrystals.[25,26] While such structural coherence has been studied extensively for PbS NCs functionalized with their native ligand oleic acid, preserving the coherence during ligand exchange is typically very challenging.[27–32] This is a clear advantage of the liquid/air assembly procedure. In contrast to most other phthalocyanines, tetraaminophthalo-cyanines are soluble in organic solvents, which allows us to apply Cu-4APc directly as part of the liquid substrate. This holds for a statistical distribution of the molecule within the NC thin film and the fabrication of a truly hybrid material with a maximized number of organic/inorganic interfaces. The potential merits of such a material are plentiful and have been reviewed previously.[14] Our electrical and photoconductance data in Fig. 3 and 4 is only one example for a future application to highlight the advantages of coupled organic–inorganic nanostructures and the challenges to overcome in the future. The AC mobility on the order of 1 cm^2 V^{-1} s^{-1} shows that efficient carrier transport in NC films with sizable tunneling barrier widths of 1.5 nm is feasible. While THz spectroscopy cannot reveal the type of mobile carrier directly, our FET measurements suggest that holes are the majority carriers, which fits the picture of resonant alignment of hole states at the interface between PbS NCs

and Cu-4APc. The DC-mobility of 10^{-3} cm^2 V^{-1} s^{-1} underlines that carrier scattering over time and length scales relevant for devices is still an issue. In consideration of our structural characterization in Fig. 1 and 2, we believe that transport within individual mesocrystalline domains is indeed efficient and responsible for the high AC mobilities. For a probing length exceeding the average grain size of 110 nm, scattering at grain boundaries and/or voids or cracks in the film inhibits carrier motion. In addition, future studies will address the question of the electronic structure at the organic/inorganic interface in PbS-Cu4APc which may not only give rise to efficient charge transfer but also to carrier trapping. If trapping is slower than $\sim$10 ps, it would only affect the FET- but not the THz-mobilities. Carrier trapping would also explain the elevated hole concentration extracted by the FET measurements. We therefore expect that further improvements of the structural coherence in the NC films and/or suppressing carrier trapping will also increase the modulation of the LET device. For the latter, the presented material is particularly appealing as variations of the NC diameter and substituting the metal center of the phthalocyanine offer many opportunities for tuning.

We use the soluble organic semiconductor Cu 4,4′,4″,4‴-tetraaminophthalocyanine to functionalize PbS nanocrystals at the liquid/air interface. These hybrid nanocrystal films are mostly monolayered and consist of mesocrystalline domains. THz spectroscopy reveals AC mobilities on the order of 1 cm^2 V^{-1} s^{-1} over length scales similar to a typical domain size. For larger length and time scales for which carrier scattering is relevant, the mobility is substantially reduced. We demonstrate the potential of phthalocyanine-capped PbS nanocrystal films for Light Effect Transistors and obtain an I_{On}/I_{Off} ratio of $\leq$250 for an unoptimized device.

TEM was performed as a user project at the Molecular Foundry, which was supported by the Office of Science, Office of Basic Energy Sciences, of the U.S. Department of Energy under Contract No. DE-AC02-05CH11231. MS acknowledges the Carl-Zeiss Foundation for a postdoctoral fellowship. J. L. acknowledges funding by Toyota Motor Europe. M. S. and F. S. thank the DFG for support under grant SCHE1905/4 and SCHR700/25.

Notes and references

1 V. M. Agranovich, Y. N. Gartstein and M. Litinskaya, *Chem. Rev.*, 2011, **111**, 5179.
2 J. Liao, S. Blok, S. J. van der Molen, S. Diefenbach, A. W. Holleitner, C. Schonenberger, A. Vladyka and M. Calame, *Chem. Soc. Rev.*, 2015, **44**, 999.
3 P. Reiss, E. Couderc, J. De Girolamo and A. Pron, *Nanoscale*, 2011, **3**, 446.
4 M. Scheele, W. Bruetting and F. Schreiber, *Phys. Chem. Chem. Phys.*, 2015, **17**, 97.
5 Q. Zhang, T. Atay, J. R. Tischler, M. S. Bradley, V. Bulovic and A. Nurmikko, *Nat. Nanotechnol.*, 2007, **2**, 555.
6 A. André, D. Zherebetskyy, D. Hanifi, B. He, M. Samadi Khoshkhoo, M. Jankowski, T. Chasse, L.-W. Wang, F. Schreiber, A. Salleo, Y. Liu and M. Scheele, *Chem. Mater.*, 2015, **27**, 8105.
7 S. Blumstengel, S. Sadofev, C. Xu, J. Puls and F. Henneberger, *Phys. Rev. Lett.*, 2006, **97**, 237401.
8 B. Ehrler, B. J. Walker, M. L. Böhm, M. W. B. Wilson, Y. Vaynzof, R. H. Friend and N. C. Greenham, *Nat. Commun.*, 2012, **3**, 1019.
9 K. Szendrei, F. Cordella, M. V. Kovalenko, M. Böberl, G. Hesser, M. Yarema, D. Jarzab, O. V. Mikhnenko, A. Gocalinska, M. Saba, F. Quochi, A. Mura, G. Bongiovanni, P. W. M. Blom, W. Heiss and M. A. Loi, *Adv. Mater.*, 2009, **21**, 683.
10 S. A. McDonald, G. Konstantatos, S. Zhang, P. W. Cyr, E. J. D. Klem, L. Levina and E. H. Sargent, *Nat. Mater.*, 2005, **4**, 138.
11 P. Nagpal and V. I. Klimov, *Nat. Commun.*, 2011, **2**, 486.
12 P. Day and M. G. Price, *J. Chem. Soc. A*, 1969, 236.
13 P. T. Day, G. Scregg and R. J. P. Williams, *Nature*, 1963, **197**, 589.
14 P. R. Brown, D. Kim, R. R. Lunt, N. Zhao, M. G. Bawendi, J. C. Grossman and V. Bulovic, *ACS Nano*, 2014, **8**, 5863.
15 M.-S. Liao and S. Scheiner, *J. Comput. Chem.*, 2002, **23**, 1391.
16 W. H. Evers, J. M. Schins, M. Aerts, A. Kulkarni, P. Capiod, M. Berthe, B. Grandidier, C. Delerue, H. S. J. van der Zant, C. van Overbeek, J. L. Peters, D. Vanmaekelbergh and L. D. A. Siebbeles, *Nat. Commun.*, 2015, **6**, 8195.
17 L. T. Kunneman, J. M. Schins, S. Pedetti, H. Heuclin, F. C. Grozema, A. J. Houtepen, B. Dubertret and L. D. A. Siebbeles, *Nano Lett.*, 2014, **14**, 7039.
18 L. T. Kunneman, M. Zanella, L. Manna, L. D. A. Siebbeles and J. M. Schins, *J. Phys. Chem. C*, 2013, **117**, 3146.
19 F. C. Grozema and L. D. A. Siebbeles, *Int. Rev. Phys. Chem.*, 2008, **27**, 87.
20 E. Hendry, M. Koeberg, J. M. Schins, L. D. A. Siebbeles and M. Bonn, *Chem. Phys. Lett.*, 2006, **432**, 441.
21 J. Zaumseil, K. W. Baldwin and J. A. Rogers, *J. Appl. Phys.*, 2003, **93**, 6117.
22 K. S. Narayan and N. Kumar, *Appl. Phys. Lett.*, 2001, **79**, 1891.
23 M. E. Gemayel, K. Börjesson, M. Herder, D. T. Duong, J. A. Hutchison, C. Ruzié, G. Schweicher, A. Salleo, Y. Geerts, S. Hecht, E. Orgiu and P. Samorí, *Nat. Commun.*, 2015, **6**, 6330.
24 T. Züchner, A. V. Failla, A. Hartschuh and A. Meixner, *J. Microsc.*, 2008, **229**, 337.
25 L. Bahrig, S. G. Hickey and A. Eychmüller, *CrystEngComm*, 2014, **16**, 9408.
26 H. Cölfen and M. Antonietti, *Angew. Chem., Int. Ed.*, 2005, **44**, 5576.
27 J. J. Choi, C. R. Bealing, K. Bian, K. J. Hughes, W. Zhang, D.-M. Smilgies, R. G. Hennig, J. R. Engstrom and T. Hanrath, *J. Am. Chem. Soc.*, 2011, **133**, 3131.
28 A. Dong, Y. Jiao and D. J. Milliron, *ACS Nano*, 2013, **7**, 10978.
29 R. Li, K. Bian, T. Hanrath, W. A. Bassett and Z. Wang, *J. Am. Chem. Soc.*, 2014, **136**, 12047.
30 J. Novak, R. Banerjee, A. Kornowski, M. Jankowski, A. André, H. Weller, F. Schreiber and M. Scheele, *ACS Appl. Mater. Interfaces*, 2016, **8**, 22526.
31 M. C. Weidman, D.-M. Smilgies and W. A. Tisdale, *Nat. Mater.*, 2016, **15**, 775.
32 M. C. Weidman, K. G. Yager and W. A. Tisdale, *Chem. Mater.*, 2015, **27**, 474.